Scalable dual in situ synthesis of polyester nanocomposites for high-energy storage

Fei-yan Luo, Yan-tong Li, Jia-yu Zhang, Li He, Jia-le Li, Nan Sun, Gui-lin Li, Yong Jiang, Ke Zhou, Qian-qian Liang, et al.

Scalable dual in situ synthesis of polyester nanocomposites for high-energy storage

Fei-Yan Luo [1], Yan-Tong Li [1], Jia-Yu Zhang [1], Li He [1], Jia-Le Li [1], Nan Sun [1], Gui-Lin Li [2], Yong Jiang [2], Ke Zhou [2], Qian-Qian Liang [2], Lei Guo [2], Hong-Yuan Wei [3], Xian-Hua Wei [1], Yuan-Lin Zhou [1], Jinkai Yuan [4], Quan-Ping Zhang *[1]

1 State Key Laboratory of Environment-friendly Energy Materials, School of Materials and Chemistry, Southwest University of Science and Technology, No. 59 Qinglong Road, Mianyang 621010, China
2 Sichuan EM Technology Co., Ltd. No. 188 Sanxing Road, Mianyang 621000, China
3 Tianjin Airtech Advanced Materials Co., Ltd. No. 161, Chagugang Town, Wuqing District, Tianjin, 301721, China
4 Sorbonne Université, CNRS, Laboratoire de Chimie de la Matière Condensée de Paris, LCMCP, UMR 7574, 75005 Paris, France

E-mail: zhangqp@swust.edu.cn

Abstract

Polymer dielectrics have extensive applications as capacitors in modern electronic and electrical systems due to their distinct merits, such as low cost, good processability, and high breakdown resistance. In the last decade, incorporating ultralow loading of nanoparticles into polymers has realized increases in dielectric constant as well as breakdown strength, thus leading to excellent capacitive performance. However, there are still a series of tough issues to be dealt with, such as the use of organic solvents, which face enormous challenges in scalable preparation. Here, a new strategy of scalable dual in situ synthesis is proposed, namely polymerization of polyethylene terephthalate (PET) synchronizes with growth of calcium borate nanoparticles, making polyester nanocomposites from monomers directly. Importantly, this route is free of organic solvents, surface modification of nanoparticles, and by-products, which is readily accessible to large-scale preparation of polyester nanocomposites. Meanwhile, uniform dispersion of as ultralow as 0.1 wt% nanoparticles and intense bonding at interfaces have been observed. Furthermore, the PET-based nanocomposite displays obvious increases in both dielectric constant and breakdown strength as compared to the neat PET. Its maximum discharged energy density reaches 15 J cm^{-3} at 690 MV m^{-1} and power density attains 218 MW cm^{-3} under 150 Ω resistance at 300 MV m^{-1}, which is far superior to the current dielectric polymers that can be produced at large scales. This work presents a scalable, safe, low-cost, and environment-friendly route toward polymer nanocomposites with extremely low filling, which carves a path to explore capacitive energy storage and other applications of polyester nanocomposites.

Keywords:

Dual in situ synthesis; Polyester nanocomposites; Dielectric energy storage

1. Introduction

Compared with electrochemical devices including batteries, fuel cells, and supercapacitors, electrostatic capacitors show intrinsic fast discharge rates (nanoseconds to microseconds) and ultrahigh power densities (10^7 to 10^8 W kg^{-1}),[1-3] which are extensively applied in modern electronics and pulsed power systems. However, the benchmark biaxially oriented polypropylene (BOPP) based capacitors display much lower energy density than their electrochemical counterparts, which causes bulk and heavy devices in electrical systems.[4, 5] Therefore, it is of great urgency and significance to produce high-energy-density polymeric materials at large scales to meet the practical increasing demands of miniaturization and integration of next-generation power systems.

The maximum stored energy density U_e is expressed as $\int_0^{P_m} EdP$, where polarization P is positively correlated to the relative permittivity ε_r and P_m represents the maximum polarization at the breakdown strength E_b (the maximum electric field that the materials can suffer before dielectric failure).[6, 7] Obviously, both ε_r and E_b play crucial roles in the energy storage of dielectrics. In addition, only a portion (U_d) of electrical energy can be discharged immediately. Discharging efficiency (η) can be expressed as $\eta = U_d/U_e$. Therefore, the coupling of high polarization, breakdown strength, and charge/discharge efficiency is desirable to improve the comprehensive energy storage performance of dielectrics.

Polymer dielectrics have distinct advantages over inorganics for uses in electrostatic capacitors, such as low cost, easy processing and high breakdown strength.[8-10] However, their weak polarizations pose a great challenge to afford the high energy storage of advanced capacitors.[11, 12] To date, a variety of approaches have been explored to enhance the polarization of polymers.[13-15] Incorporating dielectric ceramic nanoparticles into polymers seems to benefit from the large polarization of nanofillers and the high breakdown strength of polymers.[16] According to the classical theoretical models, enhanced dielectric constants of polymer nanocomposites require to blend of high loading of nanoparticles with polymers.[17, 18] However, local electric

field concentration and considerable space charges tend to be induced in the polymer nanocomposites. [19-23] Mostly, the resulting polymer nanocomposites display enhanced dielectric constants yet at the expense of largely reduced breakdown strength. [24] Therefore, an enormous challenge is to reach a compromise between dielectric constant and breakdown strength to achieve a superior energy storage density to virgin polymer matrices.

Recently, low-filling strategies of inorganic nanoparticles have been explored to raise the energy density of polymer nanocomposites. Uniform dispersion of nanoparticles (1 to 5 wt %) in polymer nanocomposites allows for alleviating local electric field concentration.[25-27] Then, enhanced breakdown strength without sacrificing dielectric constants gives rise to the desirable energy density of polymer nanocomposites. In addition, incorporating ultralow loading of nanoparticles (below 0.5 wt%) into amorphous polymer leads to obvious increases in dielectric constants. [28] Even small amounts of nanoparticles are capable of creating huge interface regions between nanoparticles and polymer chains. [29, 30] It is supposed that nanoparticles induce structural changes such as the transformation of chain conformation, formation of new chemical bonds or oriented structures at the interface regions, which are responsible for the enhanced polarization. [31-34] However, the large conduction loss at high field causes the decreases in breakdown strength of amorphous polymer nanocomposites. Alternatively, theoretical simulation indicates semicrystalline polymers display a reduced conduction loss and enhanced breakdown strength. [35, 36] Many researchers have experimentally found that its counterparts semicrystalline polymer nanocomposites show significant increases in both dielectric constants and breakdown strength.[37, 38] The ultralow loading of nanoparticles enhances deep traps, increases crystallinity, and reduces crystallite size, [36, 39] which are considered positive factors for enhanced breakdown strength. Therefore, previous studies have demonstrated that uniform dispersion of the ultralow loading of nanoparticles in semicrystalline polymer matrices is essential to high-energy storage applications.

Today, most of the work leverages the routes based on organic solvents, posing tremendous obstacles to the large-scale production of dielectric nanocomposites.

Nanoparticles or polymer matrices are preliminarily dissolved or dispersed in some organic solvents like dimethylformamide. This would require a removal stage of these solvents at a relatively high thermal treatment temperature for a long time. Despite that, it is challenging to completely remove solvents and/or impurities in polymer nanocomposites, which is detrimental to the dielectric behaviors for energy storage at high fields. In addition, the whole fabrication process involves the synthesis of polymer, surface modification of inorganic phase, and their compositing, all of which are generally performed step by step. Such complications would be explicitly incompatible with large-scale processes, particularly considering the safety and environment-friendly issues in the recovery of organic solvents.

In this work, a unique dual in situ strategy (**Figure 1a**) is proposed to achieve PET-based nanocomposites with uniform dispersion of ultralow loading of nanoparticles for dielectric energy storage. Polyester, polyethylene terephthalate (PET) is chosen as matrix because it is a typical semicrystalline polymer meanwhile displays high glass-transition temperature and high thermodynamic stability. In detail, raw calcium borate (CaB1) is first dispersed in ethylene glycol (EG) which serves as dispersion medium and one of the monomers for PET polymerization. Calcium borate ester colloid particles are formulated in EG medium due to the fact that diols tend to chemically react with borates [40, 41]. Then, the colloid solution is transferred to a 70 L steel reactor containing terephthalic acid (PTA, another monomer for the polymerization of PET) for large-scale preparation of polyester nanocomposites. During the reaction at 240 °C for 4 h, the polymerization of polyethylene terephthalate (PET) from the monomers of PTA and EG synchronizes with the growth of new calcium borate (CaB2) from the calcium borate ester. Such a fabricating route is much the same as neat PET polymerization, therefore avoiding by-products. To the best of our knowledge, this is a new processing method to make polymer nanocomposites with no need for synthesis of polymer, surface modification of nanoparticles and melt blending with screw extrusion step by step. In particular, as ultralow as 0.1 wt% of nanoparticles are uniformly dispersed in polymers using such a solvent-free route. The polyester nanocomposite displays higher dielectric

constant meanwhile breakdown strength than the neat PET, leading to superior energy storage density. This widely applicable and low-cost approach presented in this work is particularly desirable for large-scale preparation of high-energy-density polyester nanocomposites.

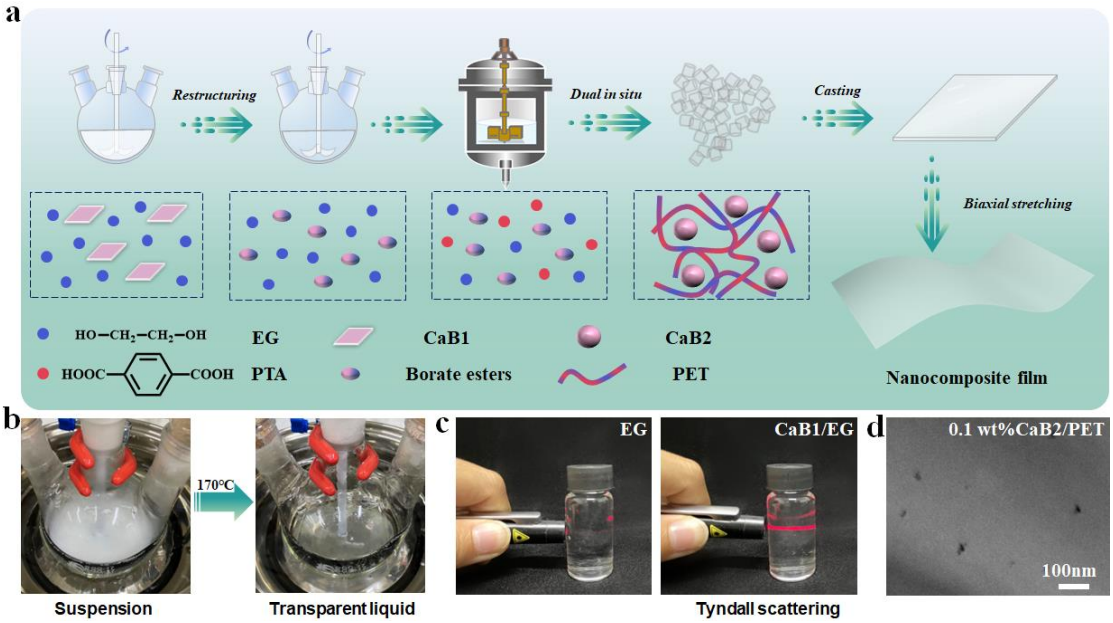

Figure 1. Schematic diagram of dual in situ route toward polyester nanocomposites. (a) Large-scale preparation of polyester nanocomposites (CaB2/PET) pellets and their thin films. (b) Formation of colloidal dispersion. (c) Tyndall scattering of CaB1/EG colloidal dispersion. (d) TEM image of CaB2/PET nanocomposite with 0.1 wt% of filler.

2. Results and discussion

Figure 1 depicts a schematic diagram of the dual in situ route toward highly scalable fabrication of polyester nanocomposite films. First, raw calcium borate (CaB1) is mixed with EG at 170 °C for 4 h. Milk white suspension was gradually transformed into a transparent liquid (**Figure 1b**). To determine the nature of the liquid, the Tyndall scattering experiment was conducted using visible light. The characteristic bright path of colloids can be clearly observed (**Figure 1c**). CaB1 has been restructured suffering from EG erosion and leading to a colloidal dispersion. The obtained colloidal dispersion is afterward added into a 70 L steel reactor containing PTA. Typical condensation polymerization occurs and leads to solid polyester nanocomposites. The PET polymerization is synchronized by the new calcium borate (CaB2) growth from the

colloidal dispersion directly. Afterward, polyester nanocomposite films were achieved by extruder casting and biaxial stretching. The proposed system is free of organic solvents, nanofiller surface modification, and melt blending with screw extrusion for polymer nanocomposites. It should be pointed out that the control system of 70 L device is identical to industrial plants, which means scalable production of polyester nanocomposites. Besides, we have found similar phenomena of colloid formulation based on Na, K, Mg, Sr, Ba, and Pb-based borates using the same treatments (**Figure S1**). Diol EG and dioic acid are the monomers of polyester polymerization. The diols tend to chemically react with borates to generate borate esters and formulate EG colloidal dispersion. Therefore, the dual in situ route tends to be extended to the scalable fabrication of polyester nanocomposites filled with a variety of borates.

As shown in **Figure 2**, we performed diverse characterizations to determine the composition of the colloidal dispersions. It is believed that boron atom usually participates in bonding in the form of sp3 or sp2 hybridization in that it has three valence electrons and four valence orbitals in the outer layer.[42] Borates can chemically react with diol units and then lead to $B(OR)_3$ borate ester and $B(OR)_4^{-1}$ complexes. [43, 44] Compared with neat EG, new absorption peaks at 937 and 960 cm^{-1} occur and the peak intensities increase with CaB1 filling (**Figure 2a**). They are characteristic peaks of the B-O bonds in $B(OR)_3$ and the bending vibration of the B-O bonds in $B(OR)_4^{-1}$ structures.[43-45] Chemical shifts of five-membered cyclic and $B(OR)_3$ structures have been detected in ^{11}B NMR (**Figure 2b**). [46, 47] After 220 ℃ vacuum treatment, the colloidal dispersion is dried into solid powders. They display similar characteristic peaks with raw CaB1 in ^{1}H NMR (**Figure 2c**). However, ^{11}B NMR and FTIR results of the solid powder indicate that the cyclic borate ester has been broken up while the $B(OR)_3$ structure remains unchanged suffering after the treatment (**Figure S2**). Moreover, according to the characteristic peaks of Raman spectra (**Figure 2d**), the borate ester shows the characteristic peaks of both CaB1 and EG. It indicates calcium is chemically bonded in the borate ester. Besides, the new absorption peak at 500 nm of wavelength and huge difference in the peaks between the reactants and the product occur in fluorescence spectra (**Figure 2e**). It further demonstrates that raw CaB1

chemically reacts with EG, leading to the borate ester. TGA curves show obvious decrease in the mass of the borate ester at the temperature range of 220 to 270 ℃ (**Figure S3**). This temperature range is suitable for PET polymerization. The mass loss is associated with the decomposition of $B(OR)_3$ and $B(OR)_4^{-1}$ feeds for the growth of new calcium borate CaB2 at the temperature range of PET polymerization. The unique dual in situ route offers the condition for CaB2 growth and PET polymerization at the same time. It can be supposed that CaB1 reacts with EG and leads to cyclic and $B(OR)_3$ borate esters and $B(OR)_4^{-1}$ complexes at 170 ℃. They are further clustered together forming colloidal dispersion. **Figure 2f** depicts the typical conductivity of the formulated colloidal dispersion, indicating that there are more charged species as a result of the proposed reaction. Namely, besides EG medium, the colloidal dispersion is composed of $B(OR)_4^{-1}$, $B(OR)_3$ and cyclic borate esters at room temperature. Nevertheless, the cyclic borate ester disappears while $B(OR)_3$ and $B(OR)_4^{-1}$ further decomposes and serves as the feed for the growth of new CaB2 nanoparticles at the elevated temperature ranges of the PET polymerization.

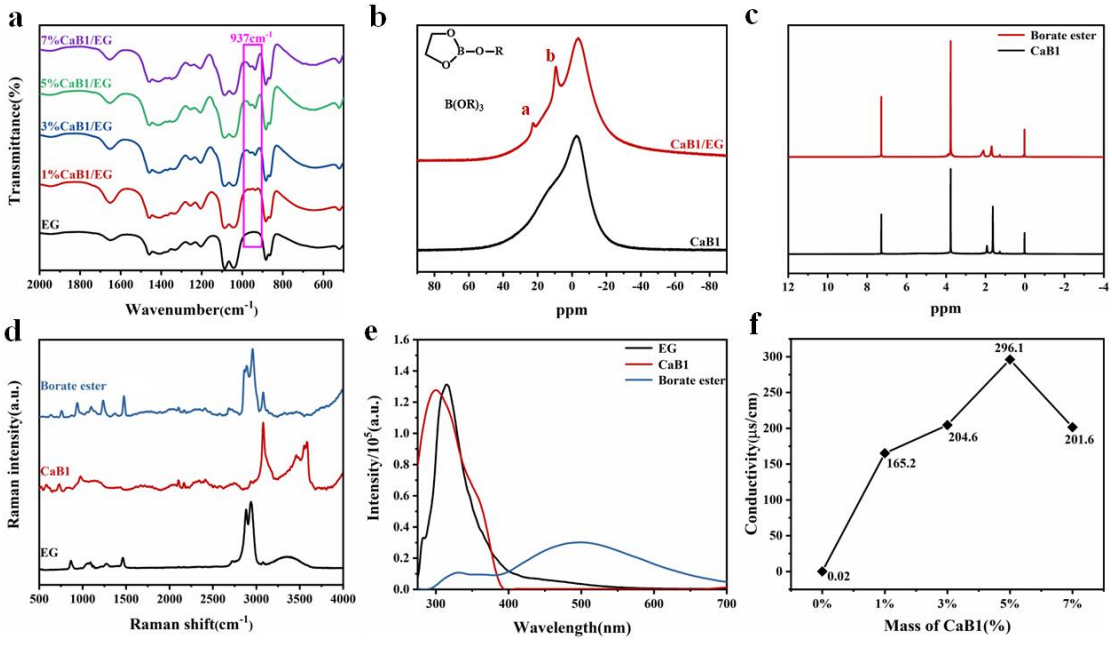

Figure 2. Characterizations of the colloidal dispersions. (a) FT-IR spectra. ^{11}B NMR (b) and ^{1}H NMR (c) of raw CaB1 and the solid borate ester from the colloidal dispersion. Raman spectra (d) and fluorescence spectra (e) of EG, raw CaB1, and the solid borate ester. (f) AC conductivity of the colloidal dispersions.

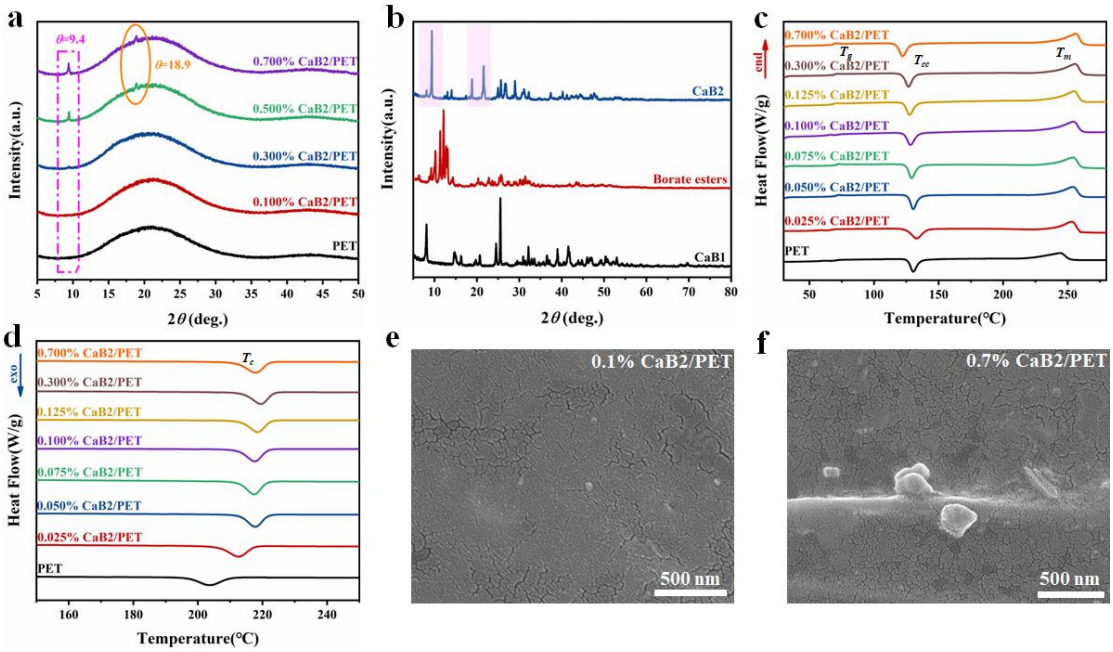

Figure 3. Characterizations of CaB2/PET nanocomposites. (a) XRD patterns of the nanocomposites with various fillings. (b) XRD patterns of raw CaB1, solid borate esters from the colloidal dispersion and CaB2 etched from the nanocomposites. DSC heating (c) and cooling (d) curves of CaB2/PET nanocomposites. SEM images of 0.1 wt% CaB2/PET nanocomposite (e) and 0.7 wt% CaB2/PET nanocomposite (f).

Figure 3 shows characterizations of CaB2/PET nanocomposites. XRD patterns show no significant differences in the diffraction peak of crystals for PET before and after introducing the filler (**Figure 3a**). New diffraction peaks at 9.4° and 18.9°can be found in XRD patterns of the nanocomposites and their intensities increase with filling. They are corresponding to the resulted CaB2 (**Figure 3b**). Interestingly, raw CaB1, resultant CaB2 and transitional calcium borate esters display entirely different absorption peaks, which indicates regrowth of new calcium borate from the transitional calcium borate esters. Obvious differences in their morphologies can also be observed (**Figure S4**). WAXS results indicate the grain size decreases from 0.01391 nm of neat PET to 0.01363 nm of 0.1 wt% CaB2/PET nanocomposite, as shown in **Figure S5**. In addition, glass transition temperature (T_g) and cold crystallization (secondary crystallization process) temperature (T_{cc}) decrease with filling (**Figure 3c**), indicating incorporation of a small amount of CaB2 promotes PET chain motion at relatively low temperatures. However, sharp increases in crystallization temperature (T_c), melting point (T_m), and degree of crystallinity are found by incorporating the ultralow fillings

(**Figure 3d**, and **Table S1**). This is because CaB2 as a nucleation agent facilitates crystallizing PET melt at relatively high temperatures and much more ordered and rigid structures tend to be formed. A small amount of CaB2 plays significant roles in PET chain motion and crystallization behavior. Besides, CaB2 is a few nanometer particles and even smaller in 0.1 wt% CaB2/PET nanocomposite (**Figure 3e**). **Figure S6** shows their sizes gradually increase from several to hundreds of nanometers with filling. Nevertheless, relatively small size of CaB2 can also be found in 0.7 wt% CaB2/PET nanocomposite (**Figure 3f**). Then the dual in situ route leads to a wide-size distribution of filler from angstrom to nanometer in 0.1 wt% CaB2/PET nanocomposites.

Figure 4 shows the dielectric properties of CaB2/PET nanocomposites. A sharp increase and then decrease in the dielectric constants with filling can be found (**Figure 4a**). The maximum value reaches $\varepsilon_r = 6.1$ at 0.1 wt% CaB2/PET nanocomposite, which is about twice that of neat PET. Meanwhile, the sample CaB2 obtained after etching their nanocomposites displays dielectric constant of about 3.8 (**Figure S7**). Note that the permittivity is boosted by a low-*k* nanofiller and at their ultralow filling with a narrow range. Previous work has tried to explain such interesting phenomenon yet no consensus has been reached. [32-39] In our case, the nanoscale CaB2, much smaller-sized nanoparticles possess a greater number of surface atoms that lack atomic coordination and have high surface energy. It displays high activity, is extremely unstable, and tends to combine with other atoms to develop new chemical bonds at the huge interface regions to enhance the dielectric polarization. Nevertheless, the sizes of CaB2 particles gradually increase from nano to micrometer with CaB1 dosage (**Figure S6**) and then their surface effects decrease, leading to the reduced permittivity at the relatively high fillings. In addition, there are weak dependences of dielectric constant and loss tangent on the frequency at room temperature (**Figure 4b** and **Figure 4c**). Importantly, the dielectric loss keeps at the same order of magnitude with neat PET although slightly fluctuates with filling. This is due to the fact that uniform dispersion of nanofillers and good compatibility at interfaces effectively inhibit mobile charge transports. Moreover, few defects tend to be formed in the nanocomposites with the dual in situ route. Meanwhile, 0.1 wt% CaB2/PET nanocomposite displays a good stability of dielectric

constant and dielectric loss below 80 ℃ while immense changes can be observed at elevated temperatures (beyond T_g), as shown in **Figure 4d** and **Figure 4e**. Besides, the breakdown probability of 0.1 wt% CaB2/PET nanocomposite film at room temperature is analyzed according to the Weibull distribution function.[48, 49] Its breakdown strength reaches 689 MV/m which is higher than that of the neat PET (663 MV/m), as shown in **Figure 4f**. Incorporating the nanofiller increases crystallinity (**Table S1**) and reduces crystallite size of the PET (**Figure S5**) [36]. Then, it restrains the mean free path for the mobile charges and enhances the deep trap level, leading to the enhanced breakdown strength.

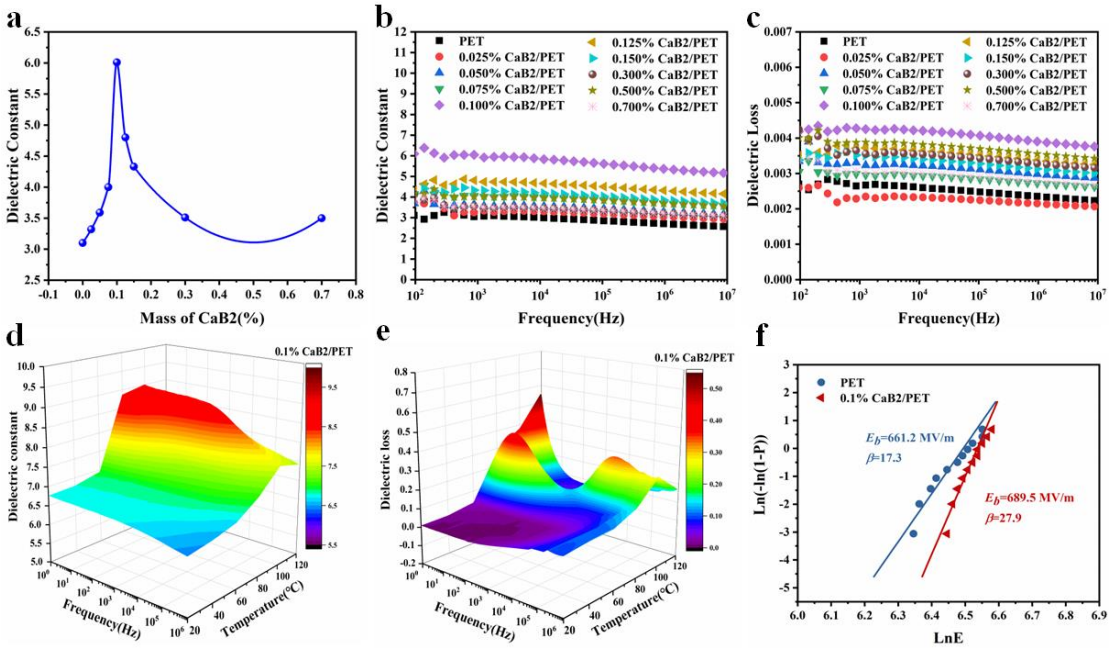

Figure 4. Dielectric properties of CaB2/PET nanocomposite films. (a) Dielectric constant as a function of filling at 1 kHz. Dielectric constant (b) and dielectric loss (c) as a function of frequency at room temperature. Dielectric constant (d) and dielectric loss (e) as a function of frequency at various temperatures. (f) Weibull distribution of dielectric breakdown failure probability.

Figure 5 shows the electrical energy storage performance of neat PET and 0.1 wt% CaB2/PET nanocomposite films. 0.1wt% CaB2/PET nanocomposite displays a higher electrical polarization than neat PET at 650 MV/m (**Figure 5a**). In particular, the maximum polarization reaches about 5 μC/cm^2 at 690 MV/m. **Figure 5b** depicts the maximum polarization (P_m) at various electrical fields, which is extracted from polarization-electric field (*P-E*) hysteresis loops (**Figure S8**). The nanocomposite

shows obvious increases in P_m value to the neat PET at high voltages. Maximum polarization subtracting remnant polarization (P_m-P_r) increases with the electrical field (**Figure 5c**). 0.1 wt% CaB2/PET nanocomposite shows 15.11 J/cm^3 of energy density at 690 MV/m, which is more than twice that of the neat PET (6.61 J/cm^3 at 650 MV/m), as shown in **Figure 5d**. Meanwhile, the charge/discharge efficiency is nearly not sacrificed and remains above 75% (**Figure 5e**). Besides, its discharged energy density remains constant over continuous 10^4 cycles of charge/discharge process (**Figure 5f**), indicating that 0.1 wt% CaB2/PET nanocomposite displays excellent electrical energy charging-discharging reliability.

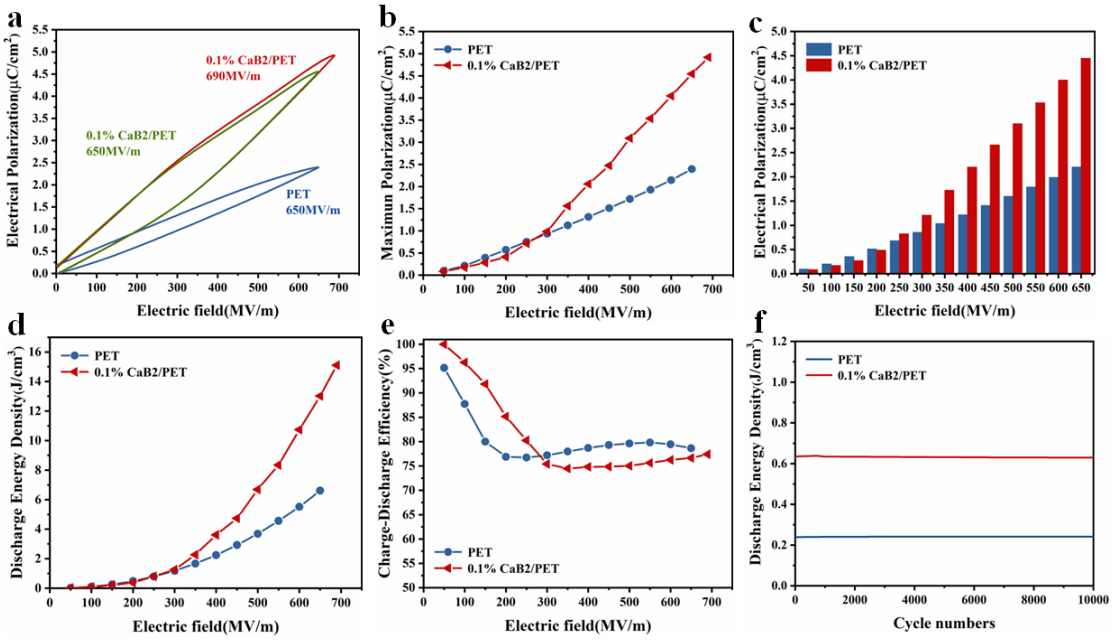

Figure 5. Electrical energy storage properties of 0.1 wt% CaB2/PET nanocomposite and neat PET films. (a) *P-E* loop at 650 and 690 MV/m. (b) Maximum polarization, (c) Maximum polarization subtracting remnant polarization (P_m-P_r), (d) Energy density and (e) Discharging efficiency at various electric fields. (f) Cyclic charge/discharge stability under 200 MV/m.

Figure 6 depicts the discharge properties of 0.1 wt% CaB2/PET nanocomposite film to evaluate the feasibility in practical application. Neat PET and BOPP films are charged at 150 MV m^{-1} and then discharged across a 150 Ω load resistor (**Figure 6a**). The discharge energy density (W_d) can be calculated from the overdamped discharge curves. [50] The W_d of PET is 0.36 J cm^{-3} and the $t_{0.9}$ (the time required to release 90% of W_d) is 13 ns, while the W_d of BOPP is 0.09 J cm^{-3} and the $t_{0.9}$ is 9 ns. At the same

loaded condition, the W_d of the nanocomposite reaches 0.45 J cm^{-3} and the $t_{0.9}$ is 22 ns. Note that the nanocomposite film is further charged at 300 MV m^{-1}. Its W_d reaches 1.49 J cm^{-3} and the $t_{0.9}$ is 23 ns. Accordingly, the nanocomposite exhibits much higher power density (49 MW cm^{-3}) than neat PET (33 MW cm^{-3}) and BOPP (26 MW cm^{-3}) at 150 MV/m. In particular, it displays superior power density of 218 MW cm^{-3} at 300 MV/m. **Figure 6b** shows the W_d monotonously increases to 1.49 J cm^{-3} and the $t_{0.9}$ maintains an ultrashort time of 23 ns with increasing the electric field. The first discharge period almost remains constant (~54 ns) under different electric fields (**Figure 6c**), indicating that the nanocomposite has rapid polarization reversal. **Figure 6d** depicts the maximum current (I_{max}), current density (C_D), and powder density (P_D) of the underdamped discharge curves as a function of electric field. Such the high W_d and P_D, ultra-high applied electric field and ultra-short $t_{0.9}$ demonstrate that 0.1 wt% CaB2/PET nanocomposite offers huge promise in application. In addition, the discharge current (**Figure 6e**) and the W_d (**Figure 6f**) slightly fluctuate with increasing temperature from 20 to 120 ℃. It further indicates that the nanocomposite has excellent stabilities of dielectric and polarization below 120 ℃.

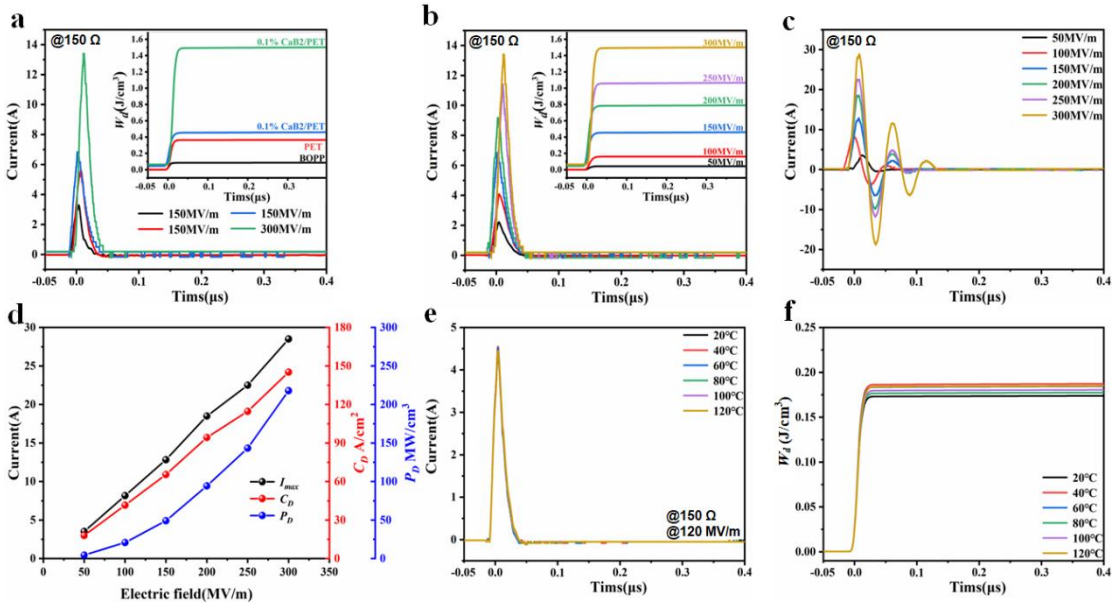

Figure 6. Discharge properties of 0.1 wt% CaB2/PET nanocomposite film. (a) Overdamped discharge curves of commercial BOPP, neat PET and this work. (b) Overdamped discharge curves (c) underdamped discharge curves, and (d) the corresponding I_{max}, C_D and P_D as a function of electric field. (e) Overdamped discharge curves and (f) discharged energy density as a function of temperature.

3. Conclusion

We propose a dual in situ strategy that crystal growth of calcium borate nanoparticles synchronizes with polyester polymerization, which realizes scalable fabrication of polyester nanocomposites from monomers directly. In particular, uniform dispersion of as ultralow as 0.1 wt% nanoparticles and intense bonding of interfaces are observed in CaB2/PET nanocomposite, leading to the most excellent electrical energy storage and discharge properties. The unique dual in situ strategy is highly adaptive to fabricate other polyester nanocomposites at large scales. In addition, it is free from solution blending with organic solvents, filler surface modification and melt blending in comparison with the common in situ and blending routes. Besides, the nanofiller geometry is potentially tuned with advanced inorganic synthesis techniques for further tailoring physical properties of polyester nanocomposites. For now, there are increasing demands for polyester materials with excellent integrated performances and used as plastic, fiber and film in advanced electronics and devices. Therefore, the scalable, safe, low-cost and environment-friendly route coupled with excellent overall performance paves a new way towards large-scale preparation of polyester nanocomposites, which offers huge promise to material design and performance development.

Supporting Information

Supporting Information is available from the Wiley Online Library or from the author.

Acknowledgments

This work was supported by the National Natural Science Foundation of China (11747042, 22309151), and the fundings from the Science & Technology Department of Sichuan Province (2022NSFSC0311, 2022JDRC0022, 2022ZHCG0135).

Conflict of Interest

There are no conflicts to declare.

References

[1] M. Yang, W. Ren, M. Guo, Y, *Small* **2022**, *18*, 202205247.
[2] X. Wu, X. Chen, Q.M. Zhang, D.Q. Tan, *Energy Storage Mater* **2022**, *44*, 29-47.
[3] Y. Shen, X. Zhang, M. Li, Y. Lin, C. W. Nan, *Natl. Sci. Rev.* **2017**, *4*, 23-25.
[4] M. Zhang, B. Li, J. J. Wang, H.-B. Huang, L. Zhang and L. Q. Chen, *Adv. Mater.* **2024**, *33*, 2008198.
[5] Q. K. Feng, S. L. Zhong, J. Y. Pei, Y. Zhao, D. L. Zhang, D. F. Liu, Y. X. Zhang, Z. M. Dang, *Chem. Rev.* **2022**, *122*, 3820-3878.
[6] J. Wei, L. Zhu, *Prog. Polym. Sci.* **2020**, *106*, 101254.
[7] H. Luo, X. Zhou, C. Ellingford, Y. Zhang, S. Chen, K. Zhou, D. Zhang, C.R. Bowen , C. Wan, *Chem. Chem. Soc. Rev.* **2019**, *48*, 4424-4465.
[8] T. Zhang, H. Sun, C. Yin, Y.H. Jung, S. Min, Y. Zhang, C. Zhang, Q. Chen, K.J. Lee , Q. Chi,. *Prog. Mater. Sci.* **2023**, *140*, 101207.
[9] H. Luo, F. Wang, R. Guo, D. Zhang, G. He, S. Chen, Q. *Adv. Sci.* **2022**, *9*, e2202438.
[10] B. Fan, M. Zhou, C. Zhang, D. He , J. Bai, *Prog. Polym. Sci.* **2019**, *97*, 101143.
[11] L. Zhu, *J. Phys. Chem. Lett. J. Phys. Chem. Lett.* **2014**, *5*, 3677-3687.
[12] Li, S. Wang, Y. Zhu, Z. Luo, Y. R. Zhang, Q. Shao, H. Quan, M. Wang, S. Hu, M. Yang, J. Fu, R. Wang, J. Hu, H. Yuan, J. He, Q. Li, *J. Mater. Chem. A*. **2023**, *11*, 10659-10668.
[13] X. Liu, F. Y. Du, J. Che, J. L. Li, A. S. Yang, J. H. Lv, Q. Y. Shen, L. He, Y. T. Li, Y. L. Zhou, J. Yuan, Q. P. Zhang, *Energy Technol.* **2022**, *11*, 2201041.
[14] J. Che, C. Zakri, I. Ly, W. Neri, E. Laurichesse, J. P. Chapel, P. Poulin, J. Yuan, *Adv. Funct. Mater.* **2023**, *33*, 202213804..
[15] S. Cheng, Y. Zhou, Y. Li, C. Yuan, M, Yang, J. Fu, J. Hu, J. He, Q. Li, *Energy Storage Mater.* **2021**, *42*, 445-453.
[16] M. Guo, J. Jiang, Z. Shen, Y. Lin, C. W. Nan, Y. Shen, *Mater. Today.* **2019**, *29*, 49-67.
[17] Prateek, V.K. Thakur, R.K. Gupta, *Chem. Rev.* **2016**, *116*, 4260-4317.
[18] B. Jiang, J. Iocozzia, L. Zhao, H. Zhang, Y.-W. Harn, Y. Chen, Z. Lin, *Chem. Soc. Rev.* **2019**, *48*, 1194-1228.
[19] X. Zhang, J. Iocozzia, L. Zhao, H. Zhang, Y. W. Harn, Y. Chen, Z. Lin, *Nanoscale* **2014**, *6*, 6701-6709.
[20] Y. U. Wang, D.Q. Tan, J. Krahn, *Appl. Phys. Lett.* **2011**, *110*, 044103.
[21] Z. H. Shen, J. J. Wang, X. Zhang, Y. Lin, C. W. Nan, L. Q. Chen, Y. Shen, *Appl. Phys. Lett.* **2017**, *111*, 092901.
[22] Z. H. Shen, Y. Shen, X. X. Cheng, H. X. Liu, L. Q. Chen, C. W. Nan, J. J. Materiomics. **2020**, *6*, 573-581.
[23] Z. Cai, X. Wang, B. Luo, W. Hong, L. Wu, L. Li, *Compos. Sci. Technol.* **2017**, *145*, 105-113.
[24] R. C. Chen, Q. P. Zhang, K. Ke N. Sun, W. D. Xu, D. L. Liu, W. Yang, Y. T. Li, Y. L. Zhou, M. B. Yang, J. Yuan, W. Yang, *J. Mater. Chem. C.* **2020**, *8*, 8786-8795.
[25] Q. Li, G. Zhang, F. Liu, K. Han, M.R. Gadinski, C. Xiong, Q. Wang, *Energy*

Environ. Sci. **2015**, *8*, 922-931.
[26] S. Ding, S. Yu; X. Zhu, S. Xie, R. Sun, W. H. Liao, C. P. Wong, *Appl. Phys. Lett.* **2017**, *111*, 153902.
[27] H. Li, D. Ai, L. Ren, B. Yao, Z. Han, Z. Shen, J. Wang, L. Q. Chen, Q. Wang, *Adv. Mater.* **2019**, *31*: 1900875.
[28] Y. Thakur, T. Zhang, C. Iacob, T. Yang, J. Bernholc, L.Q. Chen, J. Runt, Q.M. *Nanoscale* **2017**, *9*, 10992.
[29] L. S. Schadler, L.C. Brinson, W.G. Sawyer, *JOM.* **2007**, *59*, 53-60.
[30] T. Tanaka, M. Kozako, N. Fuse, Y. Ohki, *IEEE Trans. Dielectr. Electr. Insul.* **2005**, *12*, 669-681.
[31] T. Lewis, *J. Phys. D: Appl. Phys.* **2005**, *38*, 202.
[32] L. Li, J. Cheng, Y. Cheng, T. Han, Y. Liu, Y. Zhou, G. Zhao, Y. Zhao, C. Xiong, L. Dong. Q. Wang, *Adv. Mater.* **2021**, *33*, 2102392.
[33] G. Rui, J. Bernholc, S. Zhang, Q. Zhang, *Adv. Mater.* **2024**, 2311739.
[34] Y. Cheng, Y. Feng, Z. Pan, P. Wang, J. Liu, L. Liang, J. Yu, J. Zhai, Q. Wang, *Energy Environ. Sci.* **2023**, *16*, 5881-5890.
[35] C. Xu, Z. Zheng, S. A. Boggs, Conference record of the 2006 IEEE international symposium on electrical insulation **2006**, 358-361.
[36] W. Wang, D. Min, S. Li, *IEEE Trans. Dielectr. Electr. Insul.* **2016**, *23*, 564-572.
[37] F. Wang, J. Cai, C. Yang, H. Luo, X. Li, H. Hou, G. Zou, D. Zhang, *Small* **2023**, *19*, e2300510.
[38] M. Yang, S. Wang, J. Fu, Y. Zhu, J. Liang, S. Cheng, S. Hu, J. Hu, J. He, Q. Li, *Adv. Mater.* **2023**, *35*, e2301936.
[39] T. Zhang, X. Chen, Y. Thakur, B. Lu, Q. Zhang, J. Runt, Q.M. Zhang, *Sci. Adv.* **2020**, *6*, eaax6622.
[40] S.D. Bull, M.G. Davidson, J.M.H. van den Elsen, J.S. Fossey, A.T. A. Jenkins, Y. B. Jiang, Y. Kubo, F. Marken, K. Sakurai, J. Zhao, T.D. James,*Acc. Chem. Res.* **2013**, *46*, 312.
[41] A. P. Bapat, B. S. Sumerlin and A. Sutti, *Mater. Horiz.* **2020**, *7*, 694-714.
[42] W. L. A. Brooks, B.S. Sumerlin, *Chem. Rev.* **2016**, *116*, 1375-1397.
[43] C. Bai, Z. Wu, X. Ye, H. Liu, Z. Liu, H. Zhang, Q. Li, J. Li, X. Wang, *ChemistrySelect.* **2019**, *4*, 14132-14139.
[44] A. J. Hubert, B. Hargitay, J. Dale, *J. Chem. Soc.* **1961**, 192-931.
[45] L. M .S. G. A. Applegarth, C. C. Pye, J. S. Cox, P.R. Tremaine, *Ind. Eng. Chem. Res.* **2017**, *56*, 13983-13996.
[46] G. R. Eaton, *J. Chem. Educ.* **1969**, *46*, 547.
[47] J. G. Verkade, R. W. King, C.W. Heitsch, *Inorg. Chem.* **1969**, *3*, 884-889.
[48] M. Cacciari, G. Mazzanti, G.C. Montanari, *IEEE Trans. Dielectr. Electr. Insul.* **1994**, *28*, 163.
[49] V. Tomer, E. Manias, C.A. Randall, *J. Appl. Phys.* **2011**, *110*, 044107.
[50] N. Luo, K. Han, M. J. Cabral, X. Liao, S. Zhang, C. Liao, G. Zhang, X. Chen, Q. Feng, J.-F. Li, Y. Wei, *Nat. Commum.* **2020**, *11*, 4824.

Supporting Information

Scalable dual in situ synthesis of polyester nanocomposites for high-energy storage

Fei-Yan Luo [1], Yan-Tong Li [1], Jia-Yu Zhang [1], Li He [1], Jia-Le Li [1], Nan Sun [1], Gui-Lin Li [2], Yong Jiang [2], Ke Zhou [2], Qian-Qian Liang [2], Lei Guo [2], Hong-Yuan Wei [3], Xian-Hua Wei [1], Yuan-Lin Zhou [1], Jinkai Yuan [4], Quan-Ping Zhang *[1]

1 State Key Laboratory of Environment-friendly Energy Materials, School of Materials and Chemistry, Southwest University of Science and Technology, No. 59 Qinglong Road, Mianyang 621010, China
2 Sichuan EM Technology Co., Ltd. No. 188 Sanxing Road, Mianyang 621000, China
3 Tianjin Airtech Advanced Materials Co., Ltd. No. 161, Chagugang Town, Wuqing District, Tianjin, 301721, China
4 Sorbonne Université, CNRS, Laboratoire de Chimie de la Matière Condensée de Paris, LCMCP, UMR 7574, 75005 Paris, France

E-mail: zhangqp@swust.edu.cn

Methods

Materials: Calcium borate (CaB1) was purchased from Chengdu Kelong Chemical Co., Ltd. Terephthalic acid (PTA), ethylene glycol (EG) and commercial biaxial oriented polypropylene film (BOPP) were supplied by Sichuan EM Technology Co., Ltd. All materials were directly used without purification.

Dual in situ route for polyester nanocomposites: CaB1 was added into EG with intense stirring for 4 hours at 170°C. After that, the transparent liquid was mixed with PTA and catalysts for condensation polymerization of polyethylene terephthalate (PET) and growth of new calcium borate (CaB2) in 70 L steel reactor. Then, large-scale preparation of solid CaB2/PET nanocomposites was directly achieved from liquid, as shown in **Figure 1(a)**.

Film preparation: First, a single screw extruder was used for preliminary casting of the nanocomposites, leading to films with about 200 μm of thickness. Second, the prefabricated films were further processed under biaxial stretching to obtain dielectric films with about 10 μm of thickness.

Characterization and testing: Fourier infrared spectrometer (FT-IR, Nicolet iS50, USA), superconducting nuclear magnetic resonance spectrometer (Avanceow 600, Germany), steady state and transient state fluorescence spectrometer (FS5, CDJL, China) and Raman spectrometer (inVia, RenishawPIC, England) were applied to determine the structure of CaB1/EG colloidal dispersion. The conductivity of colloidal dispersion was evaluated with a DDS-307 conductivity meter (Chengdu Century Ark Technology Co., Ltd., China). X-ray diffraction analyzer (Bruker Advance D8, Germany) and differential scanning calorimetry (DSC Q2000, TA, America) were employed to analyze the structure of polyester nanocomposites. Morphological observation was performed on a field emission scanning electron microscope (SEM, JSM-7610F, JEOL, Japan) and transmission electron microscopy (TEM, Libra 200, Carl Zeiss, Germany). Dielectric properties at room temperature were measured using an impedance analyzer (4294A, Agilent, USA) while at various temperatures using another impedance analyzer (Concept 50, Novocontrol GmbH, Germany). The highest

values of dielectric constants were used to plot. The Electric breakdown strength was evaluated with a withstanding voltage tester (DDJ-50KV, Beijing Guance Jingdian Equipment Ltd, China) with an increasing voltage of 200 V s^{-1}. The hysteresis loop was measured using a TF Analyzer 3000 ferroelectric polarization tester (aixACCT Systems GmbH, Germany) at room temperature with a frequency of 10 Hz. Charge-discharge experiments involved cycling the system 10,000 times at 200 MV/m. Fast charge/discharge cycles were performed using a typical high-speed capacitor circuit with a 150 kΩ load resistor (CFD-003, TG technology, China). The WAXS test conditions were as follows: q range obtained using a French Xenocs Xeuss 3.0 wide-angle X-ray scatterometer with a copper target: $q_{min} \leqslant 0.012$ nm^{-1} , $q_{max} \geqslant 49$ nm^{-1}.

$$L = \frac{K\lambda}{\beta_{\frac{1}{2}} \cos(\theta)}$$

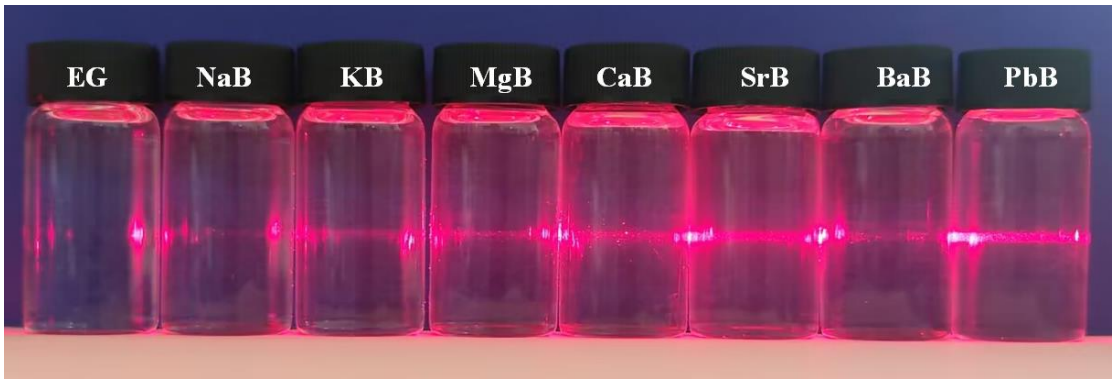

Figure S1. Tyndall scattering of colloidal dispersions with various borates.

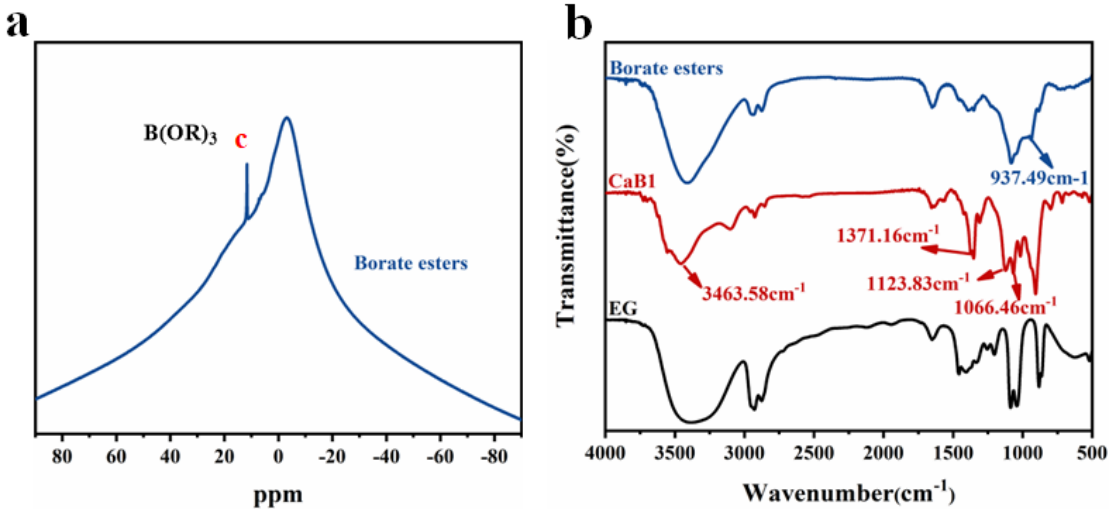

Figure S2. ^{11}B NMR and FTIR spectra of borate esters obtained after purified treatment of colloidal dispersion.

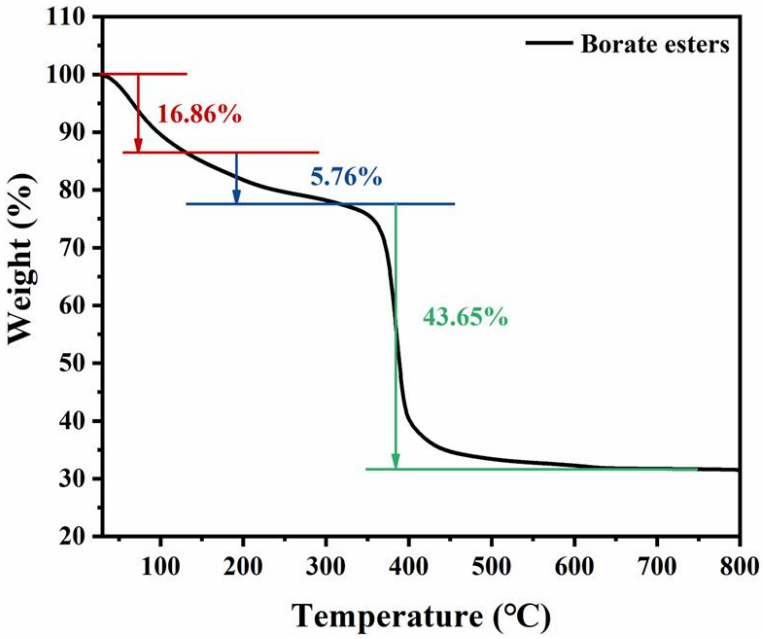

Figure S3. Borate esters obtained after purified treatment of colloidal dispersion

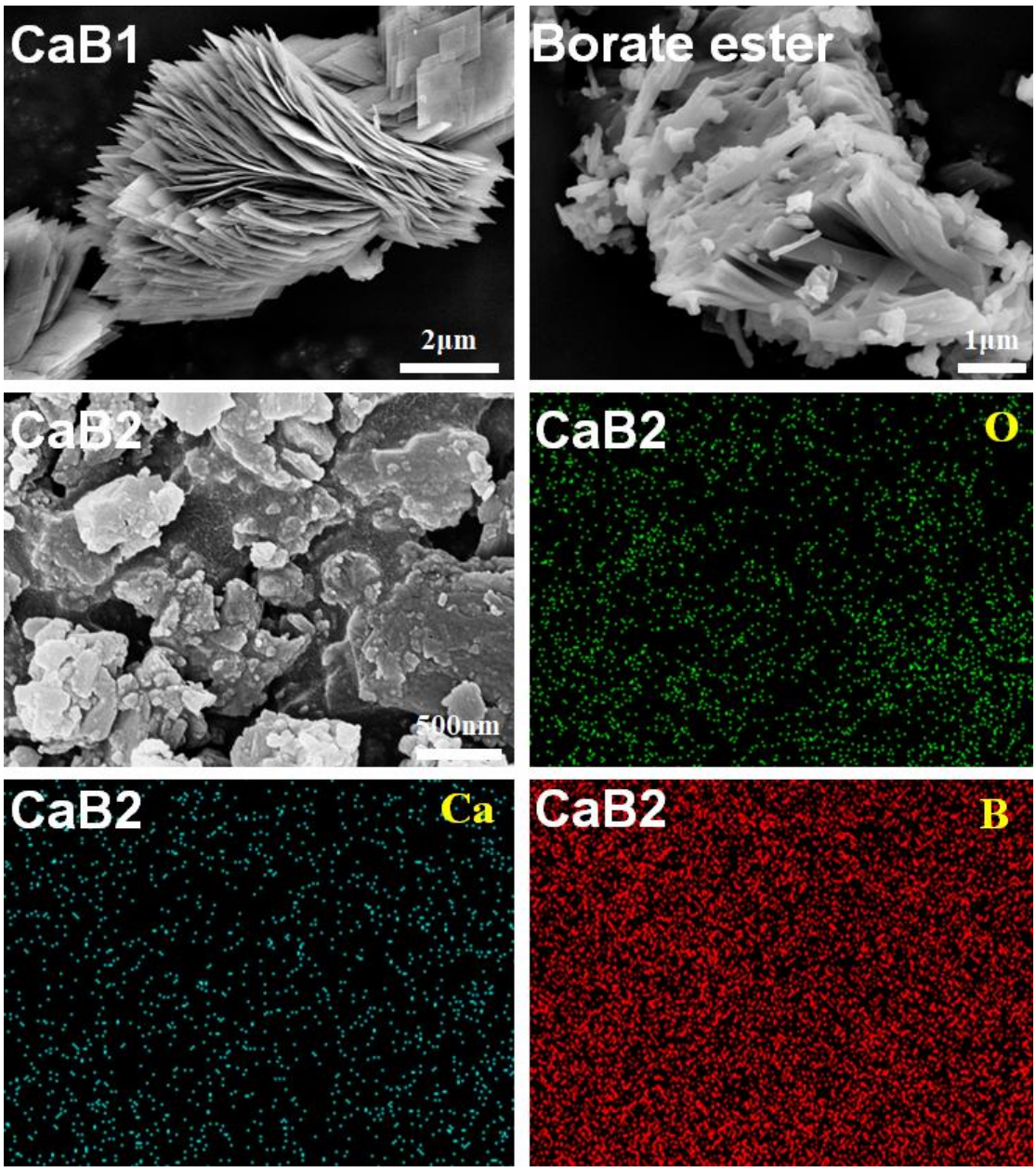

Figure S4. SEM images of CaB1, Borate esters obtained after purified treatment of colloidal dispersion, CaB2 obtained after etching the nanocomposites and the EDS results of CaB2

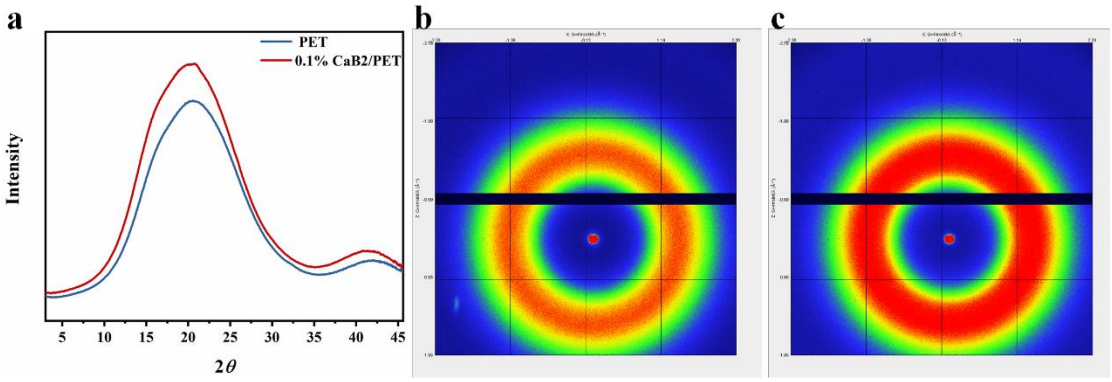

Figure S5 WAXS results of PET and 0.1% CaB2/PET nanocomposites. (a) WAXS spectra. Two-dimensional WAXS spectra of neat PET (b) and 0.1% CaB2/PET nanocomposites (c).

Table S1 DSC results of the nanocomposites and neat PET

Sample	T_g(℃)	T_{cc}(℃)	T_m(℃)	T_c(℃)	X_c(%)
PET	72.5	130.4	244.2	203.5	6.34
0.025%CBO-PET	72.4	132.9	253.5	212.5	6.51
0.050%CBO-PET	69.9	130.4	254.1	217.7	14.39
0.075%CBO-PET	70.0	129.1	254.3	217.4	19.01
0.100%CBO-PET	68.7	128.2	254.5	217.6	10.29
0.125%CBO-PET	68.5	127.5	255.0	218.5	19.15
0.150%CBO-PET	69.9	128.5	256.6	214.8	12.02
0.300%CBO-PET	69.4	126.6	255.7	219.5	15.95
0.500%CBO-PET	68.4	124.8	255.8	216.2	13.28
0.700%CBO-PET	67.6	122.1	256.2	217.8	15.35

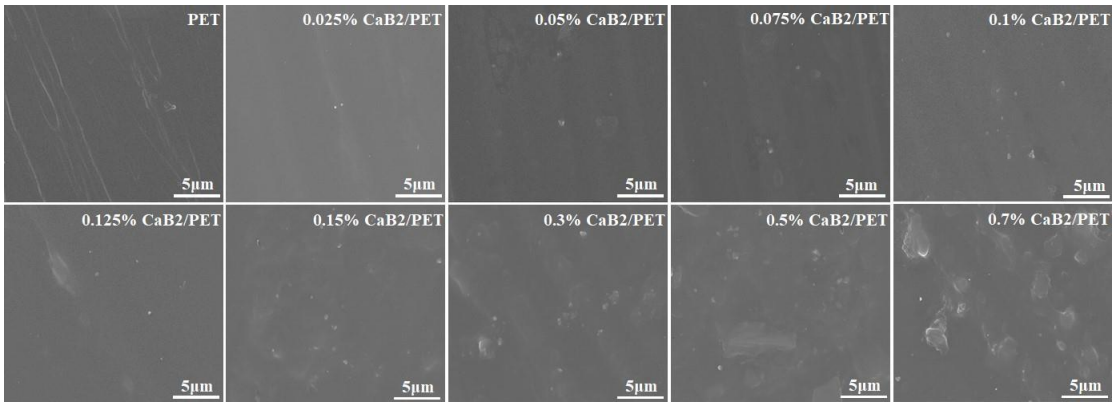

Figure S6. SEM images of CaB2/PET nanocomposites filled with various fillings

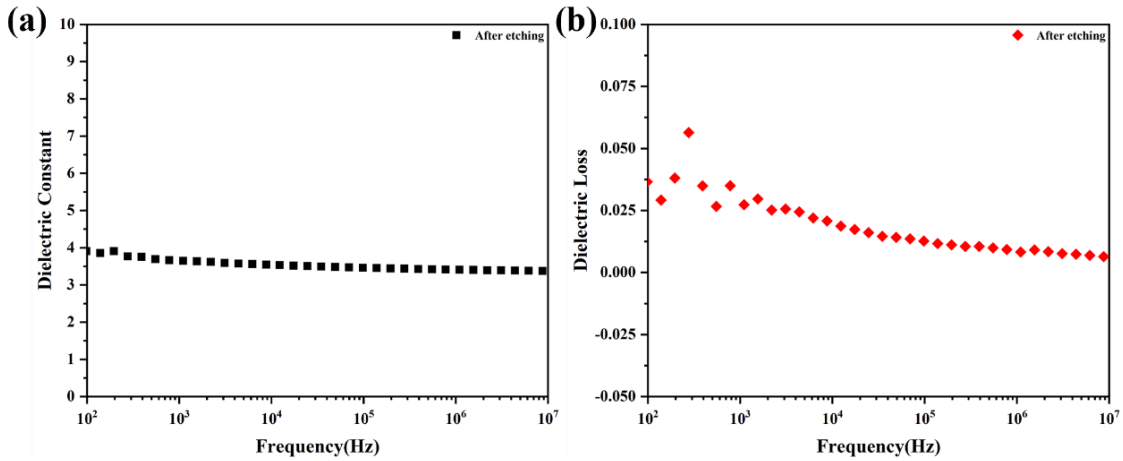

Figure S7. Dielectric constant and dielectric loss of the sample obtained after etching the nanocomposites

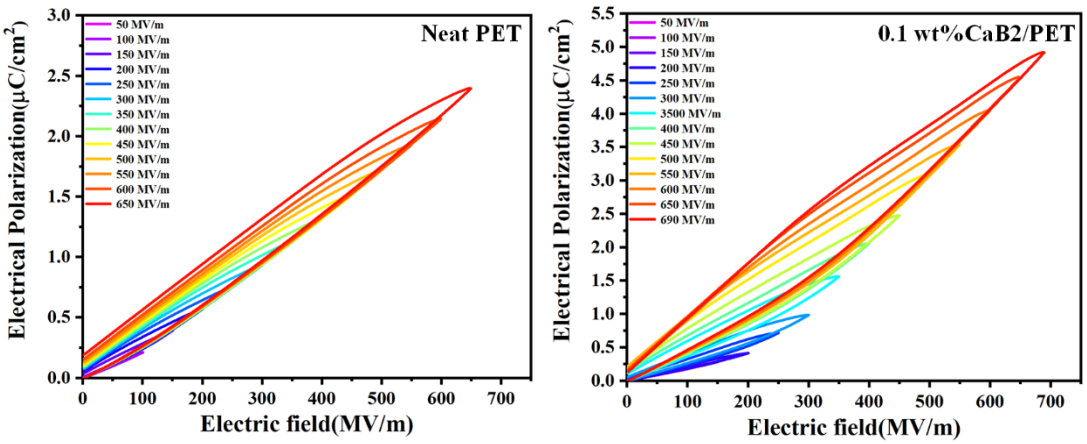

Figure S8. P-E curves of neat PET and 0.1 wt% CaB2/PET nanocomposites at various fields